Nano Research

ISSN 1998-0124 CN 11-5974/O4
https://doi.org/10.1007/s12274-022-4251-4

Research Article

Effect of ceria surface facet on stability and reactivity of isolated platinum atoms

Bochuan Song[1], Shuxin Si[1], Asiye Soleymani[1], Yan Xin[2], and Helena E. Hagelin-Weaver[1] (✉)

[1] *Department of Chemical Engineering, University of Florida, Gainesville 32611, USA*
[2] *National High Magnetic Field Laboratory, Florida State University, Tallahassee 32310, USA*

Received: 12 September 2021 / **Revised:** 8 February 2022 / **Accepted:** 18 February 2022

ABSTRACT

Well-defined surface structures and uniformity are key factors in exploring structure–activity relationships in heterogeneous catalysts. A modified atomic layer deposition method and three well-defined CeO_2 nanoshapes, octahedra with (111) surfaces, cubes exposing (100) facets, and rods with (100) and (110) surface facet terminations, were utilized to synthesize ultra-low loading Pt/CeO_2 catalysts and allow investigations on the influence of ceria surface facet on isolated Pt species under reducing conditions. A mild reduction temperature (150 °C) reduces the initial platinum ions present on the surfaces of the ceria support but preserves the isolated Pt atoms on all ceria surface facets. In contrast, a reduction temperature of 350 °C, reveals very different interactions between the initial single Pt atoms and the various ceria surface facets, leading to dissimilar and non-uniform Pt ensembles on the three ceria shapes. To isolate facet dependent Pt–CeO_2 interactions and avoid variations between Pt species, the Pt_1/CeO_2 catalysts after reduction at 150 °C were subjected to CO oxidation conditions. The isolated Pt atoms on the CeO_2 octahedra and cubes are less active in the CO oxidation reaction, compared with Pt on CeO_2 rods. In the case of Pt on the CeO_2 octahedra this is due to strongly bound CO blocking active sites together with a stable CeO_2(111) surface limiting the oxygen supply from the support. On the CeO_2 cubes, some Pt is not available for reaction and CO is bound strongly on the available Pt species. In addition, the Pt catalysts supported on the CeO_2 cubes are not stable with time on stream. The isolated Pt atoms on the CeO_2 rods are considerably more active under these conditions and this is due to a weaker Pt–CO bond strength and more facile reverse oxygen spillover from the defect-rich (110) surfaces of the rods due to the lower energy of oxygen vacancy formation on this CeO_2 surface. The Pt supported on the CeO_2 rods is also remarkably stable with time on stream. This work demonstrates the importance of using ultra-low loadings of active metal and well-defined oxide supports to isolate interactions between single metal atoms and oxide supports and determine the effects of the oxide support surface facet on the active metal at the atomic level.

KEYWORDS

single atom catalyst, CeO_2 shapes, facet effects, Pt_1/CeO_2, diffuse reflectance infrared Fourier transform spectroscopy (DRIFTS)

1 Introduction

Single atom catalysts have gained a lot of attention in recent years due to their maximized efficiency, which is particularly important when using precious metals [1, 2]. Although extensive efforts have been devoted to synthesizing single atom catalysts and evaluating their catalytic performance in various reactions, the interactions between individual metal atoms and specific surface facets of oxide supports are less well understood [3]. High surface area supports commonly used commercially in industry or in academic laboratories are generally ill-defined, and therefore add uncertainty when evaluating atomic-level structure–activity relationships of supported metal catalysts [4]. Adding to the complexity is the potential for the catalytic properties to be dependent on the metal morphology, since single atoms, small clusters, and large nanoparticles can exhibit very different catalytic activities [3, 5, 6]. Therefore, synthesizing very well-defined heterogeneous catalysts, such as single atoms of active metal on nanoparticle oxide supports with specific surface facets, has potential to reveal structure–activity relationships at an atomic level [7]. Such fundamental understanding of metal-support interactions, under different conditions is critical in the development of the next generation heterogeneous catalysts with lower cost and higher performance.

Platinum catalysts supported on cerium dioxide (CeO_2 or ceria) are widely used in many applications including automotive catalytic converters, water–gas shift reactions, and selective partial oxidation of methane, to mention a few [8–10]. Using CeO_2 as the support is beneficial due to its reduction-oxidation (redox) properties and oxygen storage capacity [11]. Therefore, as the most abundant rare earth oxide, cerium dioxide has been the subject of numerous studies over past decades [12–17]. The surface structures of CeO_2(111), (100), and (110) facets have been extensively investigated by surface science groups via both experimental and theoretical methods [18–22], and methods to synthesize well-defined CeO_2 nanoparticles with specific surface facets exposed are available in Refs. [13, 23]. Using a hydrothermal

Address correspondence to xpsun@uestc.edu.cn

synthesis strategy, ceria octahedra with (111) surface terminations, cubes with (100) surface facets, and ceria rods with either (110) and (100) facets or (111) terminations can be obtained [13]. The stability of the various CeO_2 surface facets and their reducibility are very important properties as they affect the Pt–CeO_2 interactions and thus also the catalytic activities of the resulting catalysts [24]. CeO_2(111) is the lowest energy surface and thus also the most stable surface facet which is more difficult to reduce compared with the CeO_2(110) and (100) surfaces. The CeO_2(100) surface is the least stable and can be reduced at lower temperatures compared with the CeO_2(111) surface [25]. The stability of the CeO_2(110) surface is between those of the (100) and (111) surfaces, but this surface exhibits the lowest energy of oxygen vacancy formation [23]. When comparing the three most common nanoparticle ceria shapes, the rods typically have larger surface areas compared with CeO_2 cubes and octahedra, and therefore also reveal a greater extent of reduction [26]. For these reasons, the reducibility is often reported to follow the order: (110) > (100) > (111) [23, 27], which is the reverse of the oxygen vacancy formation energies [28].

A very large number of Pt/CeO_2 catalysts have been investigated [6, 29, 30], but relatively few studies have included CeO_2 supports with well-defined shapes to investigate the influence of the CeO_2 surface facet [27, 31–33]. There are indications that the catalytic activity is dependent on the CeO_2 shape used but isolating the influence of the CeO_2 surface facet is challenging [34]. It is well known that isolated Pt^{2+} ions are very stable on CeO_2 surfaces under oxidative conditions [20, 24, 35–37]. The Pt^{2+} ions bind strongly to four oxygen ions on (100) CeO_2 facets [20, 38], and similar four-fold oxygen (O_4) sites are present at step-edges of both CeO_2 nanoparticles with predominantly (111) surfaces and CeO_2(111) single crystals [19, 38]. The single Pt ions in the O_4 pockets on CeO_2 nanoparticles are rather unreactive, as they do not adsorb CO at room temperature and are not reduced until temperatures above 400 °C [38, 39]. This is in stark contrast to small supported PtO_x clusters, which are reduced at temperatures below 100 °C [27], or even below room temperature [40–42]. Despite all the work reported on Pt/CeO_2 catalysts, a detailed investigation of Pt–CeO_2 interactions under reducing conditions and as a function of CeO_2 surface facet on ultra-low Pt loading catalysts, where Pt–CeO_2 interactions are isolated, have not been reported on CeO_2 octahedra, cubes, and rods.

To investigate metal–support interactions between isolated Pt and different CeO_2 surface facets, ultra-low loadings are critical to limit sintering and agglomeration to the extent possible, particularly under reducing conditions. It is also essential that only isolated Pt species are present, as the presence of small amounts of PtO_x clusters or even Pt dimers can greatly affect the catalytic properties [38, 43]. Under reducing conditions, the PtO_x clusters are reduced to small metallic Pt clusters at low temperature [44], and this increases the rate of hydrogen dissociation and facile hydrogen spillover results in reduction of the CeO_2 support [45]. The reduction of the CeO_2 support, in turn, reduces and destabilizes the remaining isolated Pt on the surface, and also facilitates migration of Pt across the support [20], and thus leads to formation of additional small metallic Pt particles and a very rapid increase in hydrogen uptake [44]. The presence of PtO_x clusters can therefore cause reduction of isolated Pt species at lower temperatures than if only isolated Pt ions were present on the surface [38]. Moreover, at the temperatures required for reduction of strongly bound isolated Pt^{2+} species in the O_4 pockets on CeO_2 surfaces (> 400 °C), Pt is very mobile and reduction of Pt^{2+} ions to single Pt^0 atoms or $Pt^{\delta+}$, where $\delta < 2$, without the formation of Pt nanoparticles is challenging at best.

In this work, we synthesized Pt catalysts with ultra-low loading on three CeO_2 shapes, to allow a detailed investigation of the interaction of isolated Pt species with different CeO_2 surface facets. A modified atomic layer deposition (ALD) technique was used to allow precise control over the Pt loading down to ppm levels on the different CeO_2 supports. The resulting catalysts were then carefully characterized as a function of temperature under reducing conditions using aberration-corrected high-angle-annular-dark-field scanning transmission electron microscopy (HAADF-STEM), temperature programmed reduction in 5% hydrogen (H_2-TPR), CO oxidation, and *in-situ* diffuse reflectance infrared Fourier transform spectroscopy (DRIFTS) using CO as a probe molecule to investigate the behavior of Pt on the different CeO_2 shapes, i.e., as a function of CeO_2 surface facet.

2 Experimental

2.1 Synthesis of CeO_2 nanoshapes

A template-free hydrothermal method was utilized to synthesize ceria rods, octahedra, and cubes [23]. Ceria rods or cubes were synthesized by dissolving 1.736 g of $Ce(NO_3)_3{\cdot}6H_2O$ (Fisher Scientific, Certified ACS) and 19.2 g of NaOH (Fisher Scientific, Certified ACS) in a 100 mL Teflon liner using 80 mL deionized (DI) water. After stirring vigorously for 30 min, the white slurry was sealed with a cap and transferred into a stainless-steel autoclave. The autoclave was kept in an oven for 24 h at 100 °C for rods and at 180 °C for cubes. To synthesize CeO_2 octahedra, 0.0304 g of $Na_3PO_4{\cdot}12H_2O$ (Fisher Scientific, Certified ACS) and 3.472 g of $Ce(NO_3)_3{\cdot}6H_2O$ (ACROS, 99.5%) were dissolved in 320 mL of deionized water in a 500 mL Teflon liner. After stirring vigorously for 60 min, the white solution was sealed with a cap and transferred into a stainless-steel autoclave. The autoclave was kept at 180 °C for 9.5 h inside an oven. The white precipitate of nanocrystals was separated from the supernatant by centrifugation and washed with deionized water and ethanol alternately 4 times. The resulting yellowish paste was collected in a crucible, dried in an oven overnight at 105 °C and then calcined in static air at 350 °C for 3 h.

2.2 Pt single atom deposition

The ALD process was carried out in an RX series rotary ALD reactor (ALD NanoSolutions). Trimethyl (methylcyclopentadienyl) platinum(IV) was the Pt precursor and ultrahigh purity (UHP) O_2 (Airgas, 99.999%) was used as the oxidative agent. The bubbler containing the Pt precursor was kept at 60 °C to maintain sufficient vapor pressure, and the ALD inlet line was kept at 110 °C to avoid condensation. UHP N_2 (Airgas, 99.999%) was used as the carrier gas at a 200 mL/min flow rate. In each experiment, 300 mg of ceria shapes loaded into the ALD rotary chamber and two deposition temperatures were used, 180 and 230 °C, to further tune the Pt loading. Prior to Pt deposition, a short exposure to DI water was included to ensure abundant hydroxyl groups on the CeO_2 surfaces for optimal Pt dispersion [46]. A carefully controlled dose time of 5 s was utilized to obtain an ultra-low Pt loading on the ceria supports. The dosing sequence and timings were as follows: H_2O dose (three sequential 0.2 s doses with 10 s hold and 10 s evacuation in between doses), N_2 purge (120 s), Pt precursor exposure (5 s), N_2 purge (120 s), and O_2 exposure (20 s). The as-synthesized catalysts were calcined under static air at 350 °C for 3 h to decompose the Pt precursor. The catalysts are labeled according to their CeO_2 support shape, i.e., Oct for octahedra, Cub for cubes, and Rod for the rod support, and the Pt content. This means that Cub-9.5ppm is a catalyst supported on CeO_2 cubes with a 9.5 ppm loading of Pt by weight.

2.3 Characterization

The catalysts were analyzed by inductively coupled plasma mass spectrometry (ICP-MS Perkin-Elmer Corp., Norwalk, CT) to determine the Pt loading. Each sample was measured three times and independent high-purity standards were used for the calibration curve and quality-assurance/quality control (QA/QC) protocols. Brunauer–Emmett–Teller (BET) surface area measurements were performed using a one-point isotherm on a ChemBET 3000 instrument (Quantachrome, Inc.), as described in previous publications [47]. High resolution high-angle-annular-dark-field (HAADF) scanning transmission electron microscopy (STEM) images were collected on a probe aberration-corrected JEM-ARM200 cF at 200 kV. The following experimental conditions were used: probe size 7 c, condenser lens (CL) aperture 30 μm, scan speed 32.5 μs/pixel, and camera length 8 cm, which corresponds to a probe convergence angle of 21 mrad and a collection angle of 74 mrad.

The temperature programmed reduction (TPR) experiments were also performed on the ChemBET3000 instrument. 100 mg fresh catalyst was placed inside a quartz U tube. A degassing pre-treatment was done on all the catalysts under a flow of UHP helium gas (Airgas, Inc) through the sample at a temperature of 200 °C for 20 min. After degassing, the catalyst was cooled to room temperature and gas flow was switched to UHP 5% H_2 balanced in 95% Ar (Airgas. Inc). The temperature was controlled by a tube furnace with heating rate of 10 °C/min to the set point, i.e., 350 °C. The catalysts analyzed by HAADF-STEM after reduction at 150 °C were reduced using similar conditions, i.e., in a hydrogen mixture (5% H_2 in 95% Ar) with a heating rate of 10 °C/min to the 150 °C set point. The total heating time was kept at 25 min for 150 °C reduction and 70 min in total for 350 °C reduction.

The DRIFTS measurements were conducted on a Thermo Nicolet 6700 instrument equipped with a liquid N_2 cooled Mercury–Cadmium–Telluride (MCT) detector and a high-temperature reaction chamber with ZnSe windows (Praying Mantis Harrick). All DRIFTS data were collected using 256 scans with a 4 cm^{-1} resolution. CO-DRIFTS data were collected on fresh (non-reduced) catalysts and after reduction treatment using 30 mg catalyst mixed with 270 mg KBr (ACROS, IR grade) in the sample holder. The fresh catalysts were degassed under He (Airgas, UHP) flow at 20 standard cubic centimeters per minute (sccm) for 20 min at 200 °C in the reaction chamber before cooling down to room temperature and collecting the background spectrum. The catalysts were then exposed to CO at room temperature by flowing a 5% CO mixture balanced in N_2 (Airgas, UHP) over the sample at 40 sccm for 10 min. Subsequently, He gas purging was continued at 20 sccm for 20 min to remove gas phase CO and weakly bound CO before collecting the CO-DRIFTS data. Since very little CO was adsorbed on the fresh catalysts, they were purged in 5% H_2 balanced in He (Airgas, UHP, 40 sccm) at room temperature for 10 min, before being heated to 150 °C, and then left at this temperature for 20 min. When the reduction was finished, the gas was switch back to He at 20 sccm for 10 min to purge the chamber. After cooling down to room temperature in He, the CO exposure at room temperature was repeated and CO-DRIFTS data collected on the reduced catalysts. CO-DRIFTS data were then collected as a function of temperature (in increments of 25 °C) to determine the binding strength of CO to the surface. The catalysts were first heated to 50 °C under a He flow at 20 sccm before CO-DRIFTS data were collected, then the catalysts were heated to 75 °C and CO-DRIFTS data collected and finally to 100 °C and the last set of CO-DRIFTS data were collected.

2.4 Catalyst activity test

The CO oxidation experiments were performed in a fixed bed 0.25-inch quartz tube reactor under ambient pressure. In each experiment 10 mg of catalyst was mixed with 40 mg blank CeO_2 support (same shape as the catalyst) and loaded into the tube. This low amount of catalyst was selected to avoid hot spots in the reactor and excess pressure drop. After purging in 5% H_2 balanced with Ar for 30 min at a flow rate of 50 sccm, the catalysts were heated at a rate of 10 °C/min up to 150 °C for a total duration of 40 min. The H_2 was then turned off and the catalysts allowed to cool down to room temperate under pure Ar. After reaching room temperature, the reaction gas, a mixture of 1% CO and 10% O_2 balanced with 10% Ar and 79% He at a total flow rate of 100 sccm, was introduced. The reactor outlet was continuously monitored in-real time by an on-line mass spectrometer (QGA or quantitative gas analysis, Hiden Analytical) as a function of temperature. An ice bath was used to prevent moisture from entering the QGA instrument. The CO conversion was calculated based on the partial pressure signal change of CO and CO_2.

3 Results and discussion

3.1 Catalyst synthesis

The hydrothermal synthesis method for ceria octahedra yields shapes with well-defined (111) surface facets (Fig. 1(a)), and with slightly modified conditions ceria cubes exposing exclusively (100) surface facets can be obtained (Fig. 1(c)) [13, 23]. The ceria rods were synthesized to expose mainly (110) and (100) facets (Fig. 1(e)) [11, 48]. It is important to note while the CeO_2 cubes and octahedra are very well-defined with few defects, this is not the case for the ceria rods. Numerous defects, i.e., cerium and oxygen vacancies, are visible on the surfaces of the rods (Fig. 1(e) and Fig. S1 in the Electronic Supplementary Material (ESM)) [23]. To minimize the Pt loading, a carefully controlled 5 s ALD dose of the platinum precursor was utilized. This is shorter than the saturation dose, i.e., the dose time required to saturate the surface with Pt precursors, and was selected since one ALD cycle at saturation conditions have been shown to result in Pt nanoparticles [49, 50], and longer dose times resulted in significantly higher Pt loadings [44, 51]. In this study, ultra-low loadings were utilized to maximize the interaction between the Pt and the CeO_2 surface and increase the distance between Pt atoms or ions in an attempt to avoid Pt sintering and agglomeration. As mentioned, this is particularly important under reducing conditions, as the presence of Pt (or PtO_x) clusters will initiate reduction at lower temperatures, cause hydrogen spillover, and destabilize the isolated Pt species [38]. At a deposition temperature of 180 °C, the 5 s dose time yields Pt loadings between 10–90 ppm (Table 1). The highest loading is observed on the CeO_2 nanorods. This is partly due to their higher surface area compared to the other shapes, but the rods also contain a larger number of defects, which could serve as highly reactive anchoring sites. In contrast, a deposition temperature of 230 °C results in similar and very low Pt loadings, 3 to 6.5 ppm, on all CeO_2 shapes despite their differences in surface terminations and surface areas (Table 1). These ultra-low loadings (10 ppm = 0.001% by weight) result in Pt contents that are an order of magnitude lower than typical low loading catalysts (0.01%–0.05%) [38, 52], and assures, to the extent possible, that the isolated Pt are well separated on the ceria surfaces (Figs. 1(b), 1(d), and 1(f)).

The lower Pt loading at a higher deposition temperature is unexpected, as typical ALD dose times (i.e., saturation conditions) display a nearly linear increase in Pt loading with temperature between 120 and 300 °C on various oxide supports [53]. Evidently,

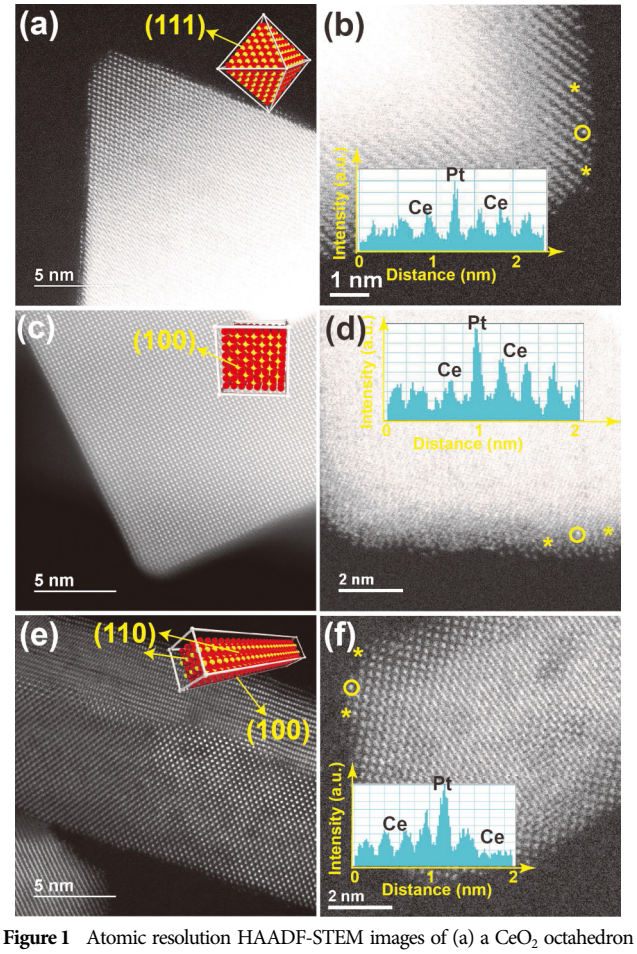

Figure 1 Atomic resolution HAADF-STEM images of (a) a CeO_2 octahedron obtained from a Pt/CeO_2-oct catalyst with a schematic of an octahedron exposing (111) surface facets, (b) fresh Oct-16ppm, (c) a CeO_2 cube obtained from a Pt/CeO_2-cub catalyst with a schematic of a cube exposing (100) surface facets, (d) fresh Cub-9.5ppm, (e) a CeO_2 rod obtained from a Pt/CeO_2-rod catalyst with a schematic of a rod exposing (110) and (100) surface facets, and (f) fresh Rod-92 ppm. Yellow circles in ((b), (d), and (f)) indicate individual Pt atoms and insets display the line intensity profile along the line between two * symbols.

Table 1 Platinum loading as a function of ALD temperature

Catalyst label	Catalyst support	Surface area (m^2/g)	ALD Temp. (°C)	ICP loading (ppm[a])
Oct-16ppm	Oct	14	180	16
Cub-9.5ppm	Cub	18	180	9.5
Rod-92ppm	Rod	67	180	92
Oct-6.5ppm	Oct	14	230	6.5
Cub-3.0ppm	Cub	18	230	3.0
Rod-5.5ppm	Rod	67	230	5.5

[a]1 ppm equals 1 mg Pt metal over 10^6 mg CeO_2.

the short dose times and the different CeO_2 surface facets exhibit a unique behavior. This may be due to removal of surface hydroxyl groups at the higher deposition temperature (230 °C) under the vacuum conditions employed during ALD. The ALD precursor reacts with surface hydroxyl groups during deposition, which facilitate precursor ligand removal and also anchor the Pt to the support [54–57]. Since the oxygen vacancy formation energies follow the order (110) < (100) < (111) [27, 58], it is expected that more hydroxyl groups would be removed from the (110) surfaces of the rods, compared with the other surfaces, leading to a more drastic difference in Pt loading between deposition temperatures on the CeO_2 rods. This may also explain why the Pt loading on the octahedra is slightly higher compared with the cubes and rods, i.e., fewer hydroxyl groups are removed, even though typical Pt ALD conditions on CeO_2 supports do not yield any Pt on the (111) surface terminations if (100) and (110) surface facets are available [51]. However, there are also indications that the reactivity of the surface hydroxyl groups on the various ceria facets different [13], which could lead to varying interactions with the ALD precursor. Finally, it is possible that the lower loading on the cubes compared with the octahedra, despite the higher surface area, is because some of the cube surfaces are cerium-terminated rather than oxygen-terminated [59], and thus have fewer anchoring sites.

3.2 Influence of reducing conditions

Since it has been shown that isolated Pt ions are not stable under reducing conditions, particularly under hydrogen atmospheres [44], the Pt/CeO_2 catalysts were reduced at low temperatures to determine the influence of the CeO_2 surface facet on the stability of the isolated Pt. Based on previously collected TPR measurements on the Pt catalysts supported on CeO_2 octahedra and cubes [60], two reduction temperatures, 150 and 350 °C, were selected for characterization using HAADF-STEM. The temperature was carefully ramped at a rate of 10 °C per minute in these experiments. A reduction temperature of 150 °C preserves the isolated Pt species on all three CeO_2 shapes (Figs. 2(a), 2(c), and 2(e)). No Pt nanoparticles can be observed in the STEM images (Fig. S2 in the ESM), consistent with previous work where lower loadings prevent sintering of isolated Pt atom [38].

After the reduction treatment at 350 °C, the high-resolution STEM images reveal that the Pt–CeO_2 interactions are highly facet dependent and the behavior of isolated Pt species on the various CeO_2 shapes is very different under these reducing conditions, as illustrated in Scheme 1. Isolated single Pt atoms are the main species on the CeO_2 octahedra after this reductive treatment (Fig. 2(b)), and only a few small and flat Pt clusters that appear to adopt the underlying (111) surface structure are present [60]. This is consistent with strong electronic metal–support interactions (EMSIs), which result in electron transfer from Pt^0 to the CeO_2 support and flat Pt clusters interacting with the (111) surface facets of CeO_2 [22, 45]. The fact that the CeO_2 (111) surfaces are not easily reduced may also play a role in providing stability for the single Pt^0 atoms on the octahedra.

In contrast, no isolated Pt atoms can be detected on the CeO_2 cubes after reduction at 350 °C, and, despite the ultra-low Pt loading, only Pt nanoparticles can be observed on this support (Fig. 2(d)). The highly stable Pt^{2+} ions on the CeO_2(100) surfaces [61], are destabilized during reduction at 350 °C, which is expected when $Pt^{\delta+}$ is reduced to Pt^0 [20]. It is also known that reduction of the CeO_2(100) surface from hydrogen spillover further destabilizes the Pt^0 and facilitates migration of Pt atoms across the (100) surfaces of CeO_2 cubes [38]. The larger three-dimensional (3D) Pt nanoparticles are likely the result of weaker interactions between the metallic Pt and CeO_2(100) compared with the CeO_2(111) surfaces.

On the CeO_2 rods, with surface facets of (110) and (100) as well as a high number of oxygen defects, the formation of two-dimensional (2D), i.e., flat, Pt particles of relatively uniform size (1–2 nm in diameter) are observed after reduction at 350 °C (Fig. 2(f). The flat Pt clusters indicate strong interactions between the Pt and the CeO_2 rod support, similar to that observed on the (111) CeO_2 surfaces of the octahedra, and is consistent with the previously reported Pt clusters observed on commercial CeO_2 support at higher Pt loadings [62]. Moreover, the flat Pt cluster adopts the facet pattern of the rod support, and they appear smaller in size compared with the Pt nanoparticles on the CeO_2 cubes. A few scattered isolated Pt species are also observed on the

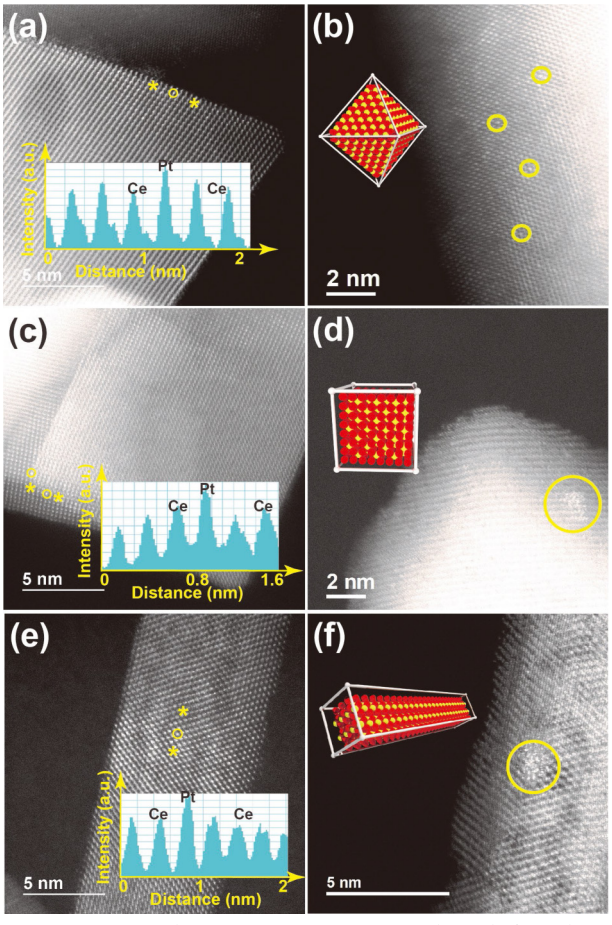

Figure 2 Atomic resolution HAADF-STEM images obtained after reduction treatment at different temperatures. (a) Oct-16ppm reduced at 150 °C, (b) Oct-16ppm reduced at 350 °C, (c) Cub-9.5ppm reduced at 150 °C, (d) Cub-9.5ppm reduced at 350 °C, (e) Rod-5.5ppm reduced at 150 °C, and (f) Rod-92ppm reduced at 350 °C.

surfaces of the rods after reduction at 350 °C, consistent with the stronger interaction between Pt and CeO_2 surface on the rods compared with the cubes. More importantly, the ratio of isolated Pt atoms to Pt clusters (or particles) is much smaller compared with the same ratio observed on the CeO_2 octahedra, where isolated Pt atoms are the dominant species after reduction. The presence of oxygen vacancies is expected to facilitate reduction of $Pt^{\delta+}$ on the CeO_2 rods [18], and the reductive treatment further leads to migration and formation of small metallic Pt nanoparticles.

3.3 Temperature programmed reduction

The H_2-TPR measurements up to 350 °C obtained from select Pt/CeO_2 catalysts are displayed in Fig. 3. TPR spectra of all catalysts and the bare supports are provided in Figs. S3–S6 in the ESM. The hydrogen consumption over these catalysts is orders of magnitude higher than expected from the Pt content with an oxidation state of Pt^{2+} or Pt^{4+} [63]. Therefore, most of the hydrogen uptake on these catalysts is due to hydrogen spillover onto the CeO_2 support. Furthermore, at a maximum reduction temperature of 350 °C, no bulk CeO_2 reduction is expected [64], so only the CeO_2 surface or near surface region is reduced. It is also evident that Pt is needed to activate the hydrogen, as very little hydrogen uptake is observed on the bare supports (Figs. S3–S5 in the ESM). The hydrogen uptake from the Oct-16ppm and Oct-6.5ppm catalysts is small (Fig. S3 in the ESM), as expected at ppm-level loadings of Pt on the most stable CeO_2 support. The TPR traces obtained from these catalysts are similar and a slight difference in signal intensity is introduced from Pt loading variance. Therefore, the data from Oct-16ppm are presented in Fig. 3, due to the higher signal-to-noise. The hydrogen uptake is very low also on the Cub-3ppm catalyst with a Pt concentration of only 3 ppm (Fig. S4 in the ESM), so the catalyst with the higher loading (Cub-9.5ppm) is presented in Fig. 3 to facilitate comparison. The first peak in the TPR spectra obtained from the Pt/CeO_2 catalysts supported on cubes and octahedra is located around 190 °C. Peaks near this temperature have been attributed to the reduction of the Pt–O–Ce bond of single $Pt^{\delta+}$ ions on CeO_2 supports [40]. The absence of peaks below 100 °C is consistent with the lack of PtO_x clusters on the fresh catalysts in this study. However, the isolated Pt species ($Pt^{\delta+}$) on both the CeO_2 cubes and the octahedra are reduced at lower temperatures compared with the isolated Pt^{2+} species located in the O_4 pockets on CeO_2 nanoparticle surfaces [38], suggesting weaker interactions between the Pt and the CeO_2 shapes in this study. This may have been expected for the CeO_2 octahedra since they lack these O_4-pocket sites but is surprising for the Pt on the CeO_2 cubes. This may suggest that the CeO_2 cubes are not thermally stable under these conditions, at least not compared with the O_4-pockets on commercial CeO_2 supports. Consistent with the more stable, and thus harder to reduce, CeO_2(111) surface [65], the hydrogen uptake is lower on the Oct-16ppm catalyst compared with the Cub-9.5ppm.

Above 300 °C there is a sharp increase in hydrogen consumption over the Cub-9.5ppm catalyst (Fig. 3). This is likely indicative of Pt particle formation with a concomitant increase in hydrogen spillover and reduction of the CeO_2(100) surface. While the initial reduction destabilizes the isolated Pt ions on the CeO_2 cubes, temperatures closer to 300 °C appear to be required to increase Pt mobility and allow Pt particle formation. This is consistent with the STEM data in Fig. 2. However, once Pt particles form, hydrogen dissociation is facile and promotes additional hydrogen spillover to the support, which causes the rapid increase in hydrogen consumption (peak at 350 °C). The

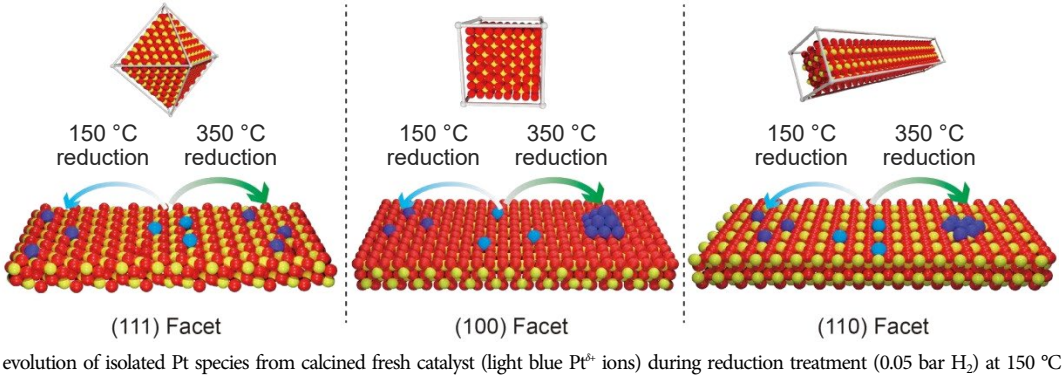

Scheme 1 The evolution of isolated Pt species from calcined fresh catalyst (light blue $Pt^{\delta+}$ ions) during reduction treatment (0.05 bar H_2) at 150 °C and 350 °C on (111) ceria surface facets (left), (100) facets (middle), and (110) facets (right). The oxygen vacancies are not included on (110). Dark blue: Pt^0, Red: O^{2-}, and Yellow: Ce^{4+}.

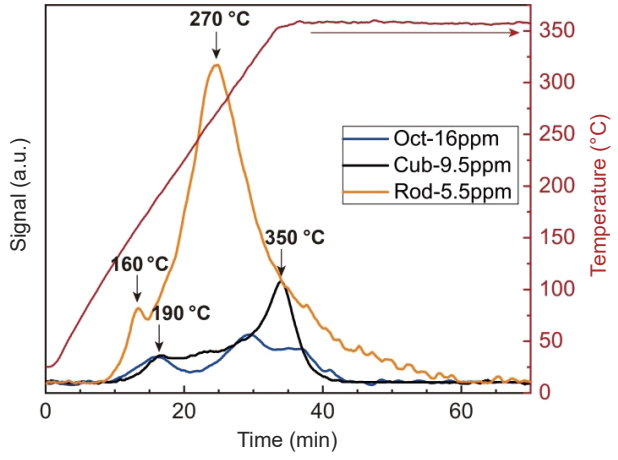

Figure 3 TPR profiles collected from catalysts, Oct-16ppm, Cub-9.5ppm, and Rod-5.5ppm. The corresponding temperature ramping profile is in dark red.

absence of a sharp peak due to Pt nanoparticle formation in the TPR spectra obtained from the Pt supported on the CeO_2 octahedra (Oct-6.5ppm and Oct-16ppm) is consistent with isolated Pt species being the predominant species observed on the CeO_2 octahedra after reduction at 350 °C.

Reduction is initiated at lower temperatures (160 °C) over the two rod-supported catalysts (Rod-5.5ppm and Rod-92ppm) compared with Pt supported on CeO_2 cubes or octahedra (Fig. 3 and Figs. S3–S5 in the ESM). The lower reduction temperature for the Rod-5.5ppm and Rod-92ppm catalysts may in part be due to the high number of defect sites on the CeO_2 rods compared with the other shapes. A very sharp increase in hydrogen consumption immediately follows the initial reduction peak. Compared with the major reduction peak obtained from the Cub-9.5ppm catalyst, the peak in the TPR spectrum obtained from the Rod-5.5ppm catalyst is substantially larger and is located at a lower temperature (270 °C). The higher hydrogen consumption and lower temperature of the major reduction peak over the Rod-5.5ppm catalyst is consistent with the lower energy of oxygen vacancy formation for the CeO_2(110) rods [23], and the larger surface area compared with the other CeO_2 shapes (Table 1). This is more evident in Fig. S6 in the ESM where the data from the bare supports are plotted on the same scale. The main difference between the two rod-supported catalysts is a higher hydrogen consumption for the Rod-92ppm catalyst, although a slight shift to lower temperatures is also observed (Fig. S5 in the ESM) compared with the Rod-5.5ppm catalyst.

3.4 The electronic properties of isolated Pt atoms

To investigate the electronic properties of isolated Pt atoms on the different CeO_2 surface facets, DRIFTS measurements were performed on fresh as well as Pt/CeO_2 catalysts reduced at 150 °C using CO as a probe molecule. CO-DRIFTS is a very sensitive tool for investigating adsorbed species down to concentrations on the order of 10^{-6} monolayers [66], and is therefore more sensitive than other surface characterization techniques, such as X-ray photoelectron spectroscopy (XPS). Furthermore, the vibrational frequency of the C=O bond of adsorbed CO molecules is highly susceptible to the local environment, i.e., the electronic structure at the adsorption site, which can help in elucidating the electronic properties of the single Pt atoms [67]. A previous study has shown that reduction of isolated Pt^{2+} ions (TPR up to 350 °C) results in electron-poor Pt species supported on CeO_2 octahedra and electron-rich Pt nanoparticles on CeO_2 cubes [60]. However, unambiguous assignment of DRIFTS peaks to specific species in that study was not possible due to the presence of more than one Pt species [68]. Therefore, all catalysts in this study were subjected to CO-DRIFTS experiments after calcination treatment and after reduction at 150 °C, where only isolated atoms were visible on the ceria shape supports.

The Oct-16ppm catalyst was selected over the Oct-6.5ppm sample, to improve the signal-to-noise. This still allows comparisons since the catalysts behave similarly and even after more harsh reduction (at 350 °C), the main difference in the CO-DRIFTS data obtained from these two catalysts is the signal intensity (Fig. S7 in the ESM). On the fresh Oct-16ppm catalyst, a small feature due to CO adsorbed on $Pt^{\delta+}$ species is observed at 2,116 cm^{-1} (Fig. 4). This is in contrast to literature observations over single Pt ions on CeO_2 nanoparticles, where no CO was adsorbed on isolated Pt^{2+} located in the O_4 pockets on the CeO_2 surfaces [38]. The Pt^{2+} species at these O_4 sites are likely coordinatively saturated and do not have available adsorption sites. However, the CeO_2 octahedra used in the current study lack these O_4 pockets, and the Pt on the (111) surfaces of the CeO_2 octahedra may instead have additional coordinated oxygens (i.e., on-top oxygens) from the calcination treatment to satisfy the requirements for coordinative saturation of surface Pt. The CO exposure at room temperature may remove some of the weakly coordinated on-top oxygens to expose an adsorption site, which would explain the observed CO adsorption. The high wavenumber of this peak is consistent with electron-poor Pt species, potentially with a coadsorbed oxygen species [69]. However, the CO-DRIFTS peak is small indicating that only a limited amount of Pt is available for CO adsorption, and no further reduction is observed with extended CO exposure at room temperature (Fig. S8 in the ESM). A low temperature reduction (150 °C) using the same reducing gas as during the TPR experiments (5% H_2 in N_2) removes additional on-top oxygens on Oct-16ppm and liberates more adsorption sites, resulting in an intensity increase of the CO-DRIFTS peak at 2,116 cm^{-1}. Reduction of the $Pt^{\delta+}$ species is also observed in a new feature at

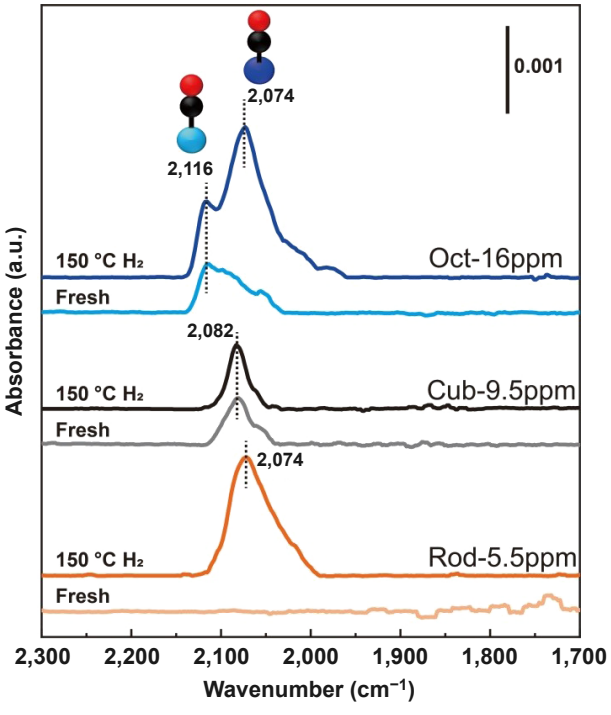

Figure 4 DRIFTS data collected from Oct-16ppm, Cub-9.5ppm, and Rod-5.5ppm catalysts after different treatments followed by exposure to CO at room temperature. Data collected after degassing with 20 sccm He flow at 200 °C for 20 min before experiments fresh and a mild reduction *in situ* 150 °C. Light blue color in cartoon indicates $Pt^{\delta+}$ and dark blue Pt^0, while black and red are carbon and oxygen of the adsorbed CO.

2,074 cm^{-1} (Fig. 4). According to most literature, CO-DRIFTS peaks at 2,074 cm^{-1} are due to CO adsorbed on relatively large Pt nanoparticles (very small nanoparticles are typically more electron rich and yield peaks at lower wavenumbers, i.e. ≤ 2,050 cm^{-1}) [38, 51]. However, CO-DRIFTS peaks between 2,075–2,065 cm^{-1} have also been assigned to single Pt atoms on CeO_2 nanorods [70]. Since no Pt nanoparticles are observed on this catalyst with STEM after reduction at 150 °C (Fig. 2 and Fig. S2 in the ESM), we assign the peak at 2,074 cm^{-1} to isolated Pt^0-like species on the CeO_2(111) surface facets. Considering the absence of detectable Pt clusters in the STEM data and the high intensity of the DRIFTS peak, it is unlikely that the 2,074 cm^{-1} peak is due to Pt nanoparticles. Also, no shift in the position of this peak due to decreasing dipole-dipole interactions with CO desorption is observed, further supporting the assignment to single atoms rather than nanoparticles (Fig. 5(a)). These Pt species are clearly more electron-rich than previously reported isolated Pt species, which are often ionic ($Pt^{\delta+}$) in nature and therefore yield CO-DRIFTS peaks at significantly higher wavenumber (> 2,085 cm^{-1}) [8, 38, 51, 71]. The ultra-low Pt loading and well-defined CeO_2 surface facets in the current study are critical to the reduction of isolated Pt^{2+} or $Pt^{\delta+}$ ions to single Pt^0 atoms without Pt agglomeration. Since CO-DRIFTS peaks at a wavenumber of 2,074 cm^{-1} have been assigned to both large Pt nanoparticles and single Pt atoms, and different Pt species can have very similar electronic environments and therefore yield DRIFTS peaks at the same wavenumbers [38, 68], the HR-STEM images after the reduction treatment (Fig. 2) are critical to the assignment of the DRIFTS peak to isolated Pt^0 instead of Pt nanoparticles on CeO_2 supports.

The signal-to-noise in the DRIFTS data obtained from the Cub-3.0ppm catalyst is also very low (Fig. S9 in the ESM), so the Cub-9.5ppm catalyst was used for these measurements (Fig. 4). Similar to the Oct-16ppm catalyst, the fresh Cub-9.5ppm sample adsorbs a small amount of CO at room temperature. However, the Pt species on the Cub-9.5ppm catalyst are more electron rich than on the Oct-16ppm catalyst, as evidenced by the red shift to 2,082 cm^{-1}. This suggests that some of the Pt^{2+} ions on the surfaces of the CeO_2 cubes are not bound as strongly as would be expected in the O_4 pockets of CeO_2(100) surfaces and that the CO exposure at room temperature is sufficient to reduce some of the Pt^{2+} on this catalyst. The peak position (2,082 cm^{-1}) suggests an electron density closer to Pt^0 (rather than $Pt^{\delta+}$) and the peak is likely due to isolated Pt atoms on the support, as the CO exposure at room temperature is not expected to induce migration of Pt across the surface to form nanoparticles [24]. This assignment is also consistent with the peak due to isolated Pt atoms near 2,074 cm^{-1} on Oct-16ppm after reduction at 150 °C. The small variation in peak position is likely caused by a CeO_2 facet effect between the (111) and (100) surfaces. It suggests that the isolated Pt on the CeO_2 (100) surfaces is slightly more electron-deficient compared with the Pt on the CeO_2(111) facets. Mild reduction at 150 °C in 5% H_2 only results in a slight increase in intensity, but the peak is narrower at 2,082 cm^{-1} peak. The small intensity change suggests that the remaining Pt^{2+} ions on the surface are difficult to reduce in agreement with previous observations of Pt^{2+} ions in the O_4 pockets of CeO_2 nanoparticles [38, 39]. This indicates that coordinatively saturated Pt^{2+} are still the primary species after hydrogen treatment at 150 °C, i.e., most of the platinum on the surface is not reduced and is therefore not available for CO adsorption.

No detectable amounts of CO molecules are adsorbed on the fresh Rod-5.5ppm catalyst (the same is true for the Rod-92ppm catalyst, Fig. S10 in the ESM), suggesting that the isolated Pt^{2+} species on the surface of this catalyst are coordinatively saturated (Fig. 4). Reduction at 150 °C, a temperature close to the first TPR

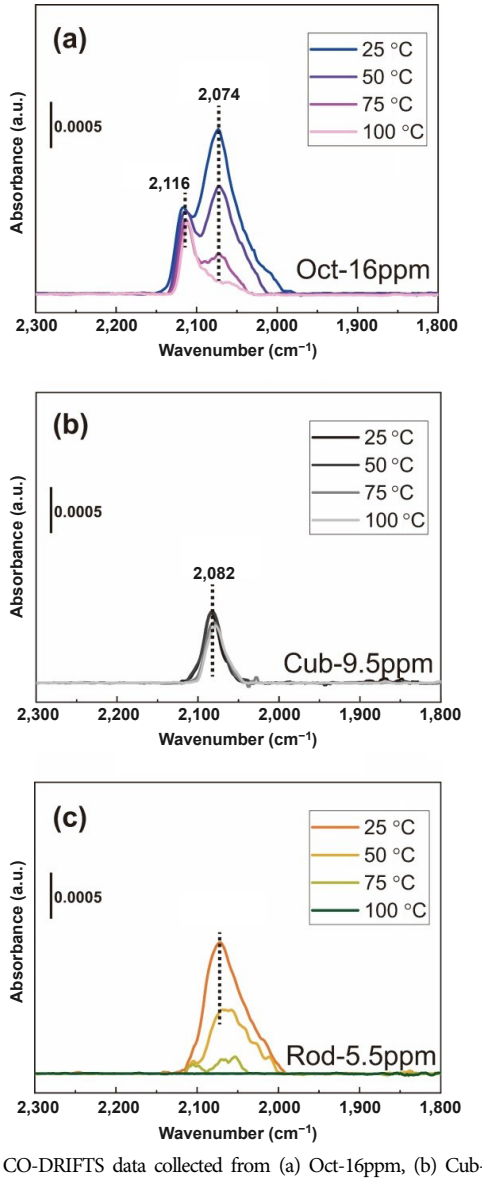

Figure 5 CO-DRIFTS data collected from (a) Oct-16ppm, (b) Cub-9.5ppm, and (c) Rod-5.5ppm catalysts after reduction at 150 °C. All samples were purged under 20 sccm He flow at each temperature for 20 min.

peak obtained from this catalyst, evidently reduces some of the isolated Pt^{2+} species on the surface of this catalyst. A peak at 2,074 cm^{-1} is introduced after reduction (Fig. 4). This is similar to the peak observed in the CO-DRIFTS measurements obtained from the catalysts supported on octahedra and cubes and is therefore assigned to isolated Pt^0 species. The lack of observable clusters in the STEM images (Fig. 2(e) and Fig. S2 in the ESM) supports this assignment since only isolated Pt species are observed on this catalyst after reduction at 150 °C. Again, this is also consistent with the isolated Pt species on CeO_2 nanorods reported in Ref. [70]. The absence of CO-DRIFTS peaks above 2,090 cm^{-1} suggests that the $Pt^{\delta+}$ species on the surface are coordinatively saturated.

The CO adsorption strength was also evaluated by heating the catalyst *in situ* and collecting CO-DRIFTS data at 50, 75 and 100 °C (Fig. 5). As expected from Ref. [8], the electron deficient $Pt^{\delta+}$ on the CeO_2 octahedra (Oct-16ppm) binds CO strongly and very little CO has desorbed from the $Pt^{\delta+}$ (2,116 cm^{-1} wavenumber) even at 100 °C (Fig. 5(a)). In contrast, the CO adsorbed on the isolated Pt^0 atoms on the Oct-16ppm catalyst (peak at 2,074 cm^{-1}) begins desorbing at 50 °C and is almost completely removed by 100 °C. Interestingly, the CO adsorbed on the isolated Pt supported on the CeO_2 cubes (peak at 2,082 cm^{-1}) is

very strongly bound. Most of the CO on the Cub-9.5ppm remains on the surface at 100 °C. In stark contrast, the CO bound to the isolated Pt^0 atoms on the CeO_2 rods (peak at 2,074 cm^{-1}) is weakly adsorbed. No detectable amount of CO remains on the Rod-5.5ppm catalyst at 100 °C.

3.5 CO oxidation of single atoms over shape supports

The CO oxidation activity of the Pt species supported on the various CeO_2 shapes was evaluated after the reduction treatment (5% H_2) at 150 °C. The reduction temperature was kept low to avoid formation of the Pt ensembles observed after reduction at 350 °C. Furthermore, non-reduced catalysts are poorly active (Fig. S11 in the ESM), as expected from the weak or non-existent CO adsorption on the fresh catalysts during the DRIFTS experiments (Fig. 4). It is evident that Pt is necessary for CO oxidation activity, even at ppm levels, as the bare supports have very little activity in this temperature range (Fig. S12 in the ESM). The catalytic activities of Pt/CeO_2 catalysts are known to be dependent on the CeO_2 shape, i.e. CeO_2 surface structure [72–75], but it is difficult to differentiate between Pt particle size effects and the influence of CeO_2 surface structure in Pt/CeO_2 catalysts with higher Pt loadings. Catalysts with ppm levels of Pt on well-defined CeO_2 supports have not been investigated previously, but this low Pt loading is necessary to determine interactions between isolated Pt atoms and specific CeO_2 facets, and how these interactions in turn affect the catalytic activity. Figure 6(a) reveals that the CO oxidation activity is dependent on the CeO_2 facet of these catalysts.

As expected from prior studies [27], the Pt species on the CeO_2 octahedra exposing (111) facets are the least active catalysts and require temperatures well above 200 °C to convert a significant amount of CO. The Oct-16ppm catalyst does not reach 100 % conversion to CO_2 until 275 °C. The poor activity of single Pt atoms over CeO_2(111) is expected, since electron-deficient platinum ($Pt^{\delta+}$) species are known to bind CO strongly, which can result in CO poisoning of the catalysts by site blocking [8, 71]. The strong CO binding is consistent with the CO-DRIFTS experiments as a function of temperature (Fig. 5(a)). Furthermore, it is well known that the CO oxidation mechanism on reducible supports involves a Mars van Krevelen mechanism in which reverse spillover of oxygen occurs from CeO_2 to Pt [8], and this is much more difficult on the low energy (111) surface facets of the more stable CeO_2 octahedra compared with other CeO_2 surfaces [23]. The low activity of the Pt catalysts supported on the CeO_2 octahedra is therefore due to the strong CO adsorption (site blocking) and the limited oxygen supply from the CeO_2 octahedra with very few defects and exclusively low-energy (111) surface facets exposed. The stability of the Pt catalysts under reaction conditions was also tested for additional 5 h at the lowest temperature where each catalyst reached 100 % conversion, as shown in Fig. S13 in the ESM. The Oct-16 ppm catalyst is remarkably stable with time on stream, indicating that isolated Pt atoms can maintain stable catalytic performance under the oxygen-rich CO oxidation conditions.

The Pt species on the CeO_2 cubes with (100) surface facets are more active at low temperatures (< 260 °C) compared with the Pt on CeO_2 octahedra. The temperature where the Cub-9.5ppm catalyst reaches 50% CO conversion (T_{50}) is 10 °C lower than for the Oct-16ppm catalyst. A higher activity is expected since the (100) surfaces of the CeO_2 cubes are more easily reduced compared with the (111) surfaces of the CeO_2 octahedra. However, few sites are available for CO adsorption on this catalyst and according to the CO-DRIFTS data the Pt sites on the CeO_2 cubes adsorb CO molecules strongly. This may explain why the Pt on the CeO_2 cubes is much less active compared with Pt on the CeO_2 rods. It may also be why the temperature where Cub-9.5ppm reaches 90% CO conversion (T_{90}) is higher than the T_{90} for the Pt supported on the CeO_2 octahedra. Furthermore, the shape of the light-off curve suggests that the Cub-9.5ppm catalyst is not stable during reaction. One explanation could be that the CeO_2(100) surfaces of the cubes are not stable and undergo reconstruction during reaction, and this could also destabilize the isolated Pt atoms [76]. This in turn may lead to sintering, i.e., Pt particle growth, and/or oxidation of Pt particles during reaction. The stability test does reveal that the Cub-9.5ppm catalyst is not stable and is exhibiting a clear deactivation trend with time on stream (Fig. S14 in the ESM).

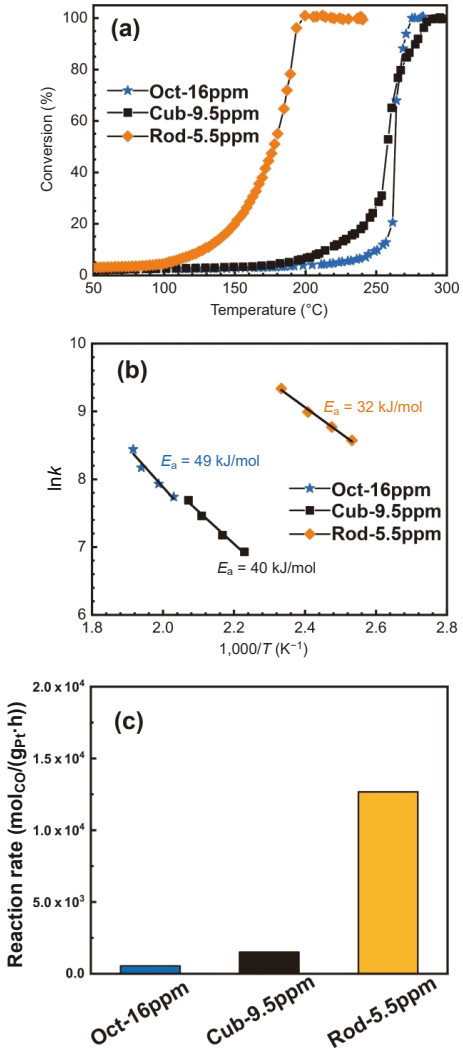

Figure 6 (a) The CO oxidation activity as a function of temperature over Oct-16ppm, Rod-5.5ppm, and Cub-9.5ppm. $CO:O_2$:Ar:He = 1:10:10:79 sccm and heating rate 10 °C/min. (b) Arrhenius plot of CO oxidation rate with calculated activation energies for the same catalysts as in (a). (c) Reaction rate in mol CO converted per gram of Pt per hour at a temperature of 190 °C.

The Pt supported on the CeO_2 rods are the most active catalysts, which is consistent with literature results [27, 70]. This is likely due to the electronic metal–support interactions on these catalysts, and the lower energy of oxygen vacancy formation, which lead to facile reverse oxygen spillover [31, 77]. Furthermore, the CO bond strength to isolated Pt species is the weakest among the three catalysts supported on the ceria shapes, as seen in Fig. 5(c). Despite having the lowest Pt loading of the three catalysts tested for activity in the CO oxidation reaction (Fig. 6), the Rod-5.5ppm catalyst is the most active. This catalyst begins to convert CO to CO_2 around 100 °C and achieve 100% conversion near 200 °C. The temperature where the Rod-5.5ppm catalyst reaches 50% conversion is 32 °C lower than for the Cub-9.5ppm catalyst.

Even though the best Pt/CeO_2 CO oxidation catalyst reported in literature reaches 100% CO conversion at a lower temperature [62], the ultra-low Pt loading catalysts in this study are remarkably active with a noble metal content that is three or four orders of magnitude lower. The stability test also demonstrated that the durability of Rod-5.5ppm under reaction conditions (Fig. S15 in the ESM). To confirm that exposure to reaction conditions does not lead to Pt particle formation, the CO-DRIFTS data were repeated for the Rod-5.5ppm and Oct-16ppm catalysts after exposure to CO oxidation inside the DRIFTS cell. No Pt particles, i.e. CO-DRIFTS peaks at lower wavenumber, were observed in either case (Figs. S16 and S17 in the ESM).

Comparing the Pt catalysts supported on the different CeO_2 shapes, it is revealed that the exposed surface facet can influence both the stability and the activity of isolated Pt atoms in the CO oxidation reaction. However, electronic interactions between the Pt and CeO_2 support is not the only factor determining the CO oxidation activity over these catalysts. Under the conditions used in this study, the oxygen supply from the support also greatly influences the overall activity. While the Pt loadings are not identical over these catalysts, it is evident that the observed differences over these catalysts are not due to variations in Pt loading. The observed effects are due to the specific CeO_2 facet exposed. The activation energies (32–49 kJ/mol) over these catalysts are in agreement with those reported in the literature (Fig. 6(b)) [31], but the CO converted per unit mass of Pt is significantly higher than previously reported values (Fig. 6(c) and Table S1 in the ESM). This reveals that the Pt is utilized very effectively on these catalysts. The single atoms of Pt on the CeO_2 rods are most active compared with the isolated Pt on the CeO_2 octahedra or cubes. This is likely due to a combination of Pt–CeO_2 interactions resulting in a weaker Pt–CO bond and the lower energy of oxygen vacancy formation on the CeO_2 rods. The results demonstrate that the exposed CeO_2 surface facet has a pronounced effect on the catalytic activity in the CO oxidation over Pt/CeO_2 catalysts.

4 Conclusions

Ultra-lo loading catalysts with isolated Pt species were synthesized by a modified ALD technique on three well-defined ceria shapes exposing different surface facets, namely octahedra with (111), cubes with (100), and rods with (100) and (110) surface facets. All three CeO_2 nanoshapes only have isolated Pt^{2+} or $Pt^{\delta+}$ species on the fresh (non-reduced) catalysts, and a mild reduction at 150 °C reduces the initial Pt ions while preserving the isolated Pt species. The Pt–CeO_2 interactions are very dependent on the specific surface facet exposed, and this is particularly evident under reducing condition. Reduction in hydrogen at 350 °C results in very different Pt ensembles on the three shapes, ranging from isolated Pt to Pt nanoparticles. To examine Pt–CeO_2 interactions as a function of CeO_2 surface facet and how these properties influence the CO oxidation reaction, the isolated Pt atoms after reduction at 150 °C were selected. Even though quantification is difficult using DRIFTS, it is likely that fewer Pt sites are available for CO oxidation over the Cub-9.5ppm catalyst (a smaller fraction of the initial Pt^{2+} species are reduced at 150 °C on the CeO_2 cubes compared with the other shapes) and, furthermore, this catalyst is not very stable. The most active catalyst is the Rod-5.5ppm and this is likely due to a weaker Pt–CO bond (more available sites for reaction) and the CeO_2(110) surfaces having the lowest energy of oxygen vacancy formation, which facilitates reverse oxygen spillover. Under the conditions used in the current study, the temperature required for 100% conversion of CO to CO_2 (175 °C) is higher than the best catalyst in in the literature [36], but, the Pt on the surface of the Rod-5.5ppm catalyst is utilized much more efficiently in the current study. The CO conversion rate per unit weight of Pt is two orders of magnitude larger than those commonly reported in the literature. This stems from not only the optimized Pt–CO bond strength on the Pt/CeO_2-rod catalysts but also efficient oxygen transfer, which is facilitated by a favorable facet effect (Pt–CeO_2 interactions) and low Pt loading. This study highlights the importance of ultra-low loadings of active metal and well-defined oxide shapes with specific surface facets exposed when investigating metal–support interactions at an atomic level.

Acknowledgements

This work was supported by the National Science Foundation (NSF) (CHE-1507230 and CBET-1933723), and the National High Magnetic Field Laboratory, which is supported by the NSF Cooperative Agreement (DMR-1644779) and the State of Florida. Startup funding from the University of Florida is also gratefully acknowledged.

Electronic Supplementary Material: Supplementary material (providing additional TEM images, DRIFTS data, and CO oxidation data) is available in the online version of this article at https://doi.org/10.1007/s12274-022-4251-4.

References

[1] Yang, X. F.; Wang, A. Q.; Qiao, B. T.; Li, J.; Liu, J. Y.; Zhang, T. Single-atom catalysts: A new frontier in heterogeneous catalysis. *Acc. Chem. Res.* **2013**, *46*, 1740–1748.

[2] Wang, A. Q.; Li, J.; Zhang, T. Heterogeneous single-atom catalysis. *Nat. Rev. Chem.* **2018**, *2*, 65–81.

[3] Li, Z.; Ji, S. F.; Liu, Y. W.; Cao, X.; Tian, S. B.; Chen, Y. J.; Niu, Z. Q.; Li, Y. D. Well-defined materials for heterogeneous catalysis: From nanoparticles to isolated single-atom sites. *Chem. Rev.* **2020**, *120*, 623–682.

[4] Dumesic, J. A.; Huber, G. W.; Boudart, M. Principles of heterogeneous catalysis: Part 1. Introduction. In *Handbook of Heterogeneous Catalysis*. Ertl, G.; Knözinger, H.; Schüth, F.; Weitkamp, J., Eds.; Wiley-VCH: Weinheim, **2008**.

[5] Lang, R.; Du, X. R.; Huang, Y. K.; Jiang, X. Z.; Zhang, Q.; Guo, Y. L.; Liu, K. P.; Qiao, B. T.; Wang, A. Q.; Zhang, T. Single-atom catalysts based on the metal–oxide interaction. *Chem. Rev.* **2020**, *120*, 11986–12043.

[6] Xin, Y.; Zhang, N. N.; Lv, Y.; Wang, J.; Li, Q.; Zhang, Z. L. From nanoparticles to single atoms for Pt/CeO_2: Synthetic strategies, characterizations and applications. *J. Rare Earths* **2020**, *38*, 850–862.

[7] J. Jones,; H. Xiong,; A.; T. DeLaRiva,; E. J. Peterson,; H. Pham,; S. R.; Challa,; G. Qi,; S. Oh,; M. H. Wiebenga,; X. I. Pereira Hernández,; Y. Wang,; A.K. Datye, Thermally stable single-atom platinum-on-ceria catalysts via atom trapping. *Science* **2016**, *353 (6295)*, 150–154.

[8] Pereira-Hernández, X. I.; DeLaRiva, A.; Muravev, V.; Kunwar, D.; Xiong, H. F.; Sudduth, B.; Engelhard, M.; Kovarik, L.; Hensen, E. J. M.; Wang, Y. et al. Tuning Pt–CeO_2 interactions by high-temperature vapor-phase synthesis for improved reducibility of lattice oxygen. *Nat. Commun.* **2019**, *10*, 1358.

[9] Xie, P. F.; Pu, T. C.; Nie, A. M.; Hwang, S.; Purdy, S. C.; Yu, W. J.; Su, D.; Miller, J. T.; Wang, C. Nanoceria-supported single-atom platinum catalysts for direct methane conversion. *ACS Catal.* **2018**, *8*, 4044–4048.

[10] Pierre, D.; Deng, W. L. Flytzani-Stephanopoulos, M. The importance of strongly bound Pt-CeO_x species for the water–gas shift reaction: Catalyst activity and stability evaluation. *Top. Catal.* **2007**, *46*, 363–373.

[11] Mai, H. X.; Sun, L. D.; Zhang, Y. W.; Si, R.; Feng, W.; Zhang, H.

P.; Liu, H. C.; Yan, C. H. Shape-selective synthesis and oxygen storage behavior of ceria nanopolyhedra, nanorods, and nanocubes. *J. Phys. Chem. B* **2005**, *109*, 24380–24385.
[12] Montini, T.; Melchionna, M.; Monai, M.; Fornasiero, P. Fundamentals and catalytic applications of CeO_2-based materials. *Chem. Rev.* **2016**, *116*, 5987–6041.
[13] Huang, W. X.; Gao, Y. X. Morphology-dependent surface chemistry and catalysis of CeO_2 nanocrystals. *Catal. Sci. Technol.* **2014**, *4*, 3772–3784.
[14] Bernal, S.; Calvino, J. J.; Cauqui, M. A.; Gatica, J. M.; Larese, C.; Omil, J. A. P.; Pintado, J. M. Some recent results on metal/support interaction effects in NM/CeO_2 (NM: noble metal) catalysts. *Catal. Today* **1999**, *50*, 175–206.
[15] Ta, N.; Liu, J. Y.; Shen, W. J. Tuning the shape of ceria nanomaterials for catalytic applications. *Chin. J. Catal.* **2013**, *34*, 838–850.
[16] Yashima, M. Invited review: Some recent developments in the atomic-scale characterization of structural and transport properties of ceria-based catalysts and ionic conductors. *Catal. Today* **2015**, *253*, 3–19.
[17] Rodriguez, J. A.; Grinter, D. C.; Liu, Z. Y.; Palomino, R. M.; Senanayake, S. D. Ceria-based model catalysts: Fundamental studies on the importance of the metal–ceria interface in CO oxidation, the water–gas shift, CO_2 hydrogenation, and methane and alcohol reforming. *Chem. Soc. Rev.* **2017**, *46*, 1824–1841.
[18] Lykhach, Y.; Figueroba, A.; Camellone, M. F.; Neitzel, A.; Skála, T.; Negreiros, F. R.; Vorokhta, M.; Tsud, N.; Prince, K. C.; Fabris, S. et al. Reactivity of atomically dispersed Pt^{2+} species towards H_2: Model Pt-CeO_2 fuel cell catalyst. *Phys. Chem. Chem. Phys.* **2016**, *18*, 7672–7679.
[19] Dvořák, F.; Farnesi Camellone, M.; Tovt, A.; Tran, N. D.; Negreiros, F. R.; Vorokhta, M.; Skála, T.; Matolínová, I.; Mysliveček, J.; Matolín, V. et al. Creating single-atom Pt-ceria catalysts by surface step decoration. *Nat. Commun.* **2016**, *7*, 10801.
[20] Bruix, A.; Lykhach, Y.; Matolínová, I.; Neitzel, A.; Skála, T.; Tsud, N.; Vorokhta, M.; Stetsovych, V.; Ševčíková, K.; Mysliveček, J. et al. Maximum noble-metal efficiency in catalytic materials: Atomically dispersed surface platinum. *Angew. Chem., Int. Ed.* **2014**, *53*, 10525–10530.
[21] Bruix, A.; Neyman, K. M.; Illas, F. Adsorption, oxidation state, and diffusion of Pt atoms on the CeO_2(111) surface. *J. Phys. Chem. C* **2010**, *114*, 14202–14207.
[22] Senanayake, S. D.; Rodriguez, J. A.; Stacchiola, D. Electronic metal–support interactions and the production of hydrogen through the water–gas shift reaction and ethanol steam reforming: Fundamental studies with well-defined model catalysts. *Top. Catal.* **2013**, *56*, 1488–1498.
[23] Wu, Z. L.; Li, M. J.; Howe, J.; Meyer III, H. M., Overbury, S. H. Probing defect sites on CeO_2 nanocrystals with well-defined surface planes by Raman spectroscopy and O_2 adsorption. *Langmuir* **2010**, *26*, 16595–16606.
[24] Maurer, F.; Jelic, J.; Wang, J. J.; Gänzler, A.; Dolcet, P.; Wöll, C.; Wang, Y. M.; Studt, F.; Casapu, M.; Grunwaldt, J. D. Tracking the formation, fate and consequence for catalytic activity of Pt single sites on CeO_2. *Nat. Catal.* **2020**, *3*, 824–833.
[25] Paier, J.; Penschke, C.; Sauer, J. Oxygen defects and surface chemistry of ceria: Quantum chemical studies compared to experiment. *Chem. Rev.* **2013**, *113*, 3949–3985.
[26] Zhou, Q. Y.; Zhou, C. Y.; Zhou, Y. H.; Hong, W.; Zou, S. H.; Gong, X. Q.; Liu, J. J.; Xiao, L. P.; Fan, J. More than oxygen vacancies: A collective crystal-plane effect of CeO_2 in gas-phase selective oxidation of benzyl alcohol. *Catal. Sci. Technol.* **2019**, *9*, 2960–2967.
[27] Gao, Y. X.; Wang, W. D.; Chang, S. J.; Huang, W. X. Morphology effect of CeO_2 support in the preparation, metal–support interaction, and catalytic performance of Pt/CeO_2 catalysts. *ChemCatChem* **2013**, *5*, 3610–3620.
[28] Nolan, M. Enhanced oxygen vacancy formation in ceria (111) and (110) surfaces doped with divalent cations. *J. Mater. Chem.* **2011**, *21*, 9160–9168.
[29] Mori, T.; Ou, D. R.; Zou, J.; Drennan, J. Present status and future prospect of design of Pt-cerium oxide electrodes for fuel cell applications. *Prog. Nat. Sci. Mater. Int.* **2012**, *22*, 561–571.
[30] Palma, V.; Ruocco, C.; Cortese, M.; Renda, S.; Meloni, E.; Festa, G.; Martino, M. Platinum based catalysts in the water gas shift reaction: Recent advances. *Metals* **2020**, *10*, 866.
[31] Singhania, N.; Anumol, E. A.; Ravishankar, N.; Madras, G. Influence of CeO_2 morphology on the catalytic activity of CeO_2-Pt hybrids for CO oxidation. *Dalton Trans.* **2013**, *42*, 15343–15354.
[32] Wu, T. X.; Pan, X. Q.; Zhang, Y. B.; Miao, Z. Z.; Zhang, B.; Li, J. W.; Yang, X. G. Investigation of the redispersion of Pt nanoparticles on polyhedral ceria nanoparticles. *J. Phys. Chem. Lett.* **2014**, *5*, 2479–2483.
[33] Safonova, O. V.; Guda, A. A.; Paun, C.; Smolentsev, N.; Abdala, P. M.; Smolentsev, G.; Nachtegaal, M.; Szlachetko, J.; Soldatov, M. A.; Soldatov, A. V. et al. Electronic and geometric structure of Ce^{3+} forming under reducing conditions in shaped ceria nanoparticles promoted by platinum. *J. Phys. Chem. C* **2014**, *118*, 1974–1982.
[34] Torrente-Murciano, L.; Garcia-Garcia, F. R. Effect of nanostructured support on the WGSR activity of Pt/CeO_2 catalysts. *Catal. Commun.* **2015**, *71*, 1–6.
[35] Kunwar, D.; Zhou, S. L.; DeLaRiva, A.; Peterson, E. J.; Xiong, H. F.; Pereira-Hernández, X. I.; Purdy, S. C.; ter Veen, R.; Brongersma, H. H.; Miller, J. T. et al. Stabilizing high metal loadings of thermally stable platinum single atoms on an industrial catalyst support. *ACS Catal.* **2019**, *9*, 3978–3990.
[36] Nie, L.; Mei, D. H.; Xiong, H. F.; Peng, B.; Ren, Z. B.; Hernandez, X. I. P.; DeLaRiva, A.; Wang, M.; Engelhard, M. H.; Kovarik, L. et al. Activation of surface lattice oxygen in single-atom Pt/CeO_2 for low-temperature CO oxidation. *Science* **2017**, *358*, 1419–1423.
[37] Tovt, A.; Bagolini, L.; Dvořák, F.; Tran, N. D.; Vorokhta, M.; Beranová, K.; Johánek, V.; Camellone, M. F.; Skála, T.; Matolínová, I. et al. Ultimate dispersion of metallic and ionic platinum on ceria. *J. Mater. Chem. A* **2019**, *7*, 13019–13028.
[38] Resasco, J.; DeRita, L.; Dai, S.; Chada, J. P.; Xu, M. J.; Yan, X. X.; Finzel, J.; Hanukovich, S.; Hoffman, A. S.; Graham, G. W. et al. Uniformity is key in defining structure–function relationships for atomically dispersed metal catalysts: The case of Pt/CeO_2. *J. Am. Chem. Soc.* **2020**, *142*, 169–184.
[39] Zhang, S. C.; Chen, L. N.; Qi, Z. Y.; Zhuo, L.; Chen, J. L.; Pao, C. W.; Su, J.; Somorjai, G. A. Insights into the mechanism of *n*-hexane reforming over a single-site platinum catalyst. *J. Am. Chem. Soc.* **2020**, *142*, 16533–16537.
[40] Ke, J.; Zhu, W.; Jiang, Y. Y.; Si, R.; Wang, Y. J.; Li, S. C.; Jin, C. H.; Liu, H. C.; Song, W. G.; Yan, C. H. et al. Strong local coordination structure effects on subnanometer PtO_x clusters over CeO_2 nanowires probed by low-temperature CO oxidation. *ACS Catal.* **2015**, *5*, 5164–5173.
[41] Dutta, G.; Waghmare, U. V.; Baidya, T.; Hegde, M. S. Hydrogen spillover on CeO_2/Pt: Enhanced storage of active hydrogen. *Chem. Mater.* **2007**, *19*, 6430–6436.
[42] Chen, J. Y.; Wanyan, Y. J.; Zeng, J. X.; Fang, H. H.; Li, Z. J.; Dong, Y. D.; Qin, R. X.; Wu, C. Z.; Liu, D. Y.; Wang, M. Z. et al. Surface engineering protocol to obtain an atomically dispersed Pt/CeO_2 catalyst with high activity and stability for CO oxidation. *ACS Sustainable Chem. Eng.* **2018**, *6*, 14054–14062.
[43] Wang, H.; Liu, J. X.; Allard, L. F.; Lee, S.; Liu, J. L.; Li, H.; Wang, J. Q.; Wang, J.; Oh, S. H.; Li, W. et al. Surpassing the single-atom catalytic activity limit through paired Pt–O–Pt ensemble built from isolated Pt_1 atoms. *Nat. Commun.* **2019**, *10*, 3808.
[44] Ye, X. X.; Wang, H. W.; Lin, Y.; Liu, X. Y.; Cao, L. N.; Gu, J.; Lu, J. L. Insight of the stability and activity of platinum single atoms on ceria. *Nano Res.* **2019**, *12*, 1401–1409.
[45] Bruix, A.; Migani, A.; Vayssilov, G. N.; Neyman, K. M.; Libuda, J.; Illas, F. Effects of deposited Pt particles on the reducibility of CeO_2(111). *Phys. Chem. Chem. Phys.* **2011**, *13*, 11384–11392.
[46] Feng, H.; Libera, J. A.; Stair, P. C.; Miller, J. T.; Elam, J. W. Subnanometer palladium particles synthesized by atomic layer deposition. *ACS Catal.* **2011**, *1*, 665–673.
[47] Jones, A. S.; Aziz, D.; Ilsemann, J.; Bäumer, M.; Hagelin-Weaver,

H. Effects of low molar concentrations of low-valence dopants on samarium oxide xerogels in the oxidative coupling of methane. *Catal. Today* **2021**, *365*, 58–70.

[48] Liu, X. W.; Zhou, K. B.; Wang, L.; Wang, B. Y.; Li, Y. D. Oxygen vacancy clusters promoting reducibility and activity of ceria nanorods. *J. Am. Chem. Soc.* **2009**, *131*, 3140–3141.

[49] Wang, C. D.; Hu, L. H.; Poeppelmeier, K.; Stair, P. C.; Marks, L. Nucleation and growth process of atomic layer deposition platinum nanoparticles on strontium titanate nanocuboids. *Nanotechnology* **2017**, *28*, 185704.

[50] Wang, H.; Lu, J. L.; Marshall, C. L.; Elam, J. W.; Miller, J. T.; Liu, H. B.; Enterkin, J. A.; Kennedy, R. M.; Stair, P. C.; Poeppelmeier, K. R. et al. *In situ* XANES study of methanol decomposition and partial oxidation to syn-gas over supported Pt catalyst on $SrTiO_3$ nanocubes. *Catal. Today* **2014**, *237*, 71–79.

[51] Wang, C. L.; Gu, X. K.; Yan, H.; Lin, Y.; Li, J. J.; Liu, D. D.; Li, W. X.; Lu, J. L. Water-mediated mars-van krevelen mechanism for CO oxidation on ceria-supported single-atom Pt_1 catalyst. *Acs Catal.* **2017**, *7*, 887–891.

[52] DeRita, L.; Dai, S.; Lopez-Zepeda, K.; Pham, N.; Graham, G. W.; Pan, X. Q.; Christopher, P. Catalyst architecture for stable single atom dispersion enables site-specific spectroscopic and reactivity measurements of CO adsorbed to Pt atoms, oxidized Pt clusters, and metallic Pt clusters on TiO_2. *J. Am. Chem. Soc.* **2017**, *139*, 14150–14165.

[53] Wang, C. D.; Hu, L. H.; Lin, Y. Y.; Poeppelmeier, K.; Stair, P.; Marks, L. Controllable ALD synthesis of platinum nanoparticles by tuning different synthesis parameters. *J. Phys. D Appl. Phys.* **2017**, *50*, 415301.

[54] Lu, J. L.; Elam, J. W.; Stair, P. C. Atomic layer deposition—Sequential self-limiting surface reactions for advanced catalyst "bottom-up" synthesis. *Surf. Sci. Rep.* **2016**, *71*, 410–472.

[55] Stair, P. C. Synthesis of supported catalysts by atomic layer deposition. *Top. Catal.* **2012**, *55*, 93–98.

[56] Yan, H.; Cheng, H.; Yi, H.; Lin, Y.; Yao, T.; Wang, C. L.; Li, J. J.; Wei, S. Q.; Lu, J. L. Single-atom Pd_1/graphene catalyst achieved by atomic layer deposition: Remarkable performance in selective hydrogenation of 1, 3-butadiene. *J. Am. Chem. Soc.* **2015**, *137*, 10484–10487.

[57] Lu, J. L.; Elam, J. W.; Stair, P. C. Synthesis and stabilization of supported metal catalysts by atomic layer deposition. *Acc. Chem. Res.* **2013**, *46*, 1806–1815.

[58] Nolan, M.; Parker, S. C.; Watson, G. W. The electronic structure of oxygen vacancy defects at the low index surfaces of ceria. *Surf. Sci.* **2005**, *595*, 223–232.

[59] Lin, Y. Y.; Wu, Z. L.; Wen, J. G.; Poeppelmeier, K. R.; Marks, L. D. Imaging the atomic surface structures of CeO_2 nanoparticles. *Nano Lett.* **2014**, *14*, 191–196.

[60] Song, B. C.; Choi, D.; Xin, Y.; Bowers, C. R.; Hagelin-Weaver, H. Ultra-low loading Pt/CeO_2 catalysts: Ceria facet effect affords improved pairwise selectivity for parahydrogen enhanced NMR spectroscopy. *Angew. Chem., Int. Ed.* **2021**, *60*, 4038–4042.

[61] Aleksandrov, H. A.; Neyman, K. M.; Vayssilov, G. N. The structure and stability of reduced and oxidized mononuclear platinum species on nanostructured ceria from density functional modeling. *Phys. Chem. Chem. Phys.* **2015**, *17*, 14551–14560.

[62] Gatla, S.; Aubert, D.; Agostini, G.; Mathon, O.; Pascarelli, S.; Lunkenbein, T.; Willinger, M. G.; Kaper, H. Room-temperature CO oxidation catalyst: Low-temperature metal–support interaction between platinum nanoparticles and nanosized ceria. *ACS Catal.* **2016**, *6*, 6151–6155.

[63] Daelman, N.; Capdevila-Cortada, M.; López, N. Dynamic charge and oxidation state of Pt/CeO_2 single-atom catalysts. *Nat. Mater.* **2019**, *18*, 1215–1221.

[64] Gao, Y. X.; Li, R. T.; Chen, S. L.; Luo, L. F.; Cao, T.; Huang, W. X. Morphology-dependent interplay of reduction behaviors, oxygen vacancies and hydroxyl reactivity of CeO_2 nanocrystals. *Phys. Chem. Chem. Phys.* **2015**, *17*, 31862–31871.

[65] Huang, W. X. Oxide nanocrystal model catalysts. *Acc. Chem. Res.* **2016**, *49*, 520–527.

[66] Van Every, K. W.; Griffiths, P. R. Characterization of diffuse reflectance FT-IR spectrometry for heterogeneous catalyst studies. *Appl. Spectrosc.* **1991**, *45*, 347–359.

[67] DeRita, L.; Resasco, J.; Dai, S.; Boubnov, A.; Thang, H. V.; Hoffman, A. S.; Ro, I.; Graham, G. W.; Bare, S. R.; Pacchioni, G. et al. Structural evolution of atomically dispersed Pt catalysts dictates reactivity. *Nat. Mater.* **2019**, *18*, 746–751.

[68] Aleksandrov, H. A.; Neyman, K. M.; Hadjiivanov, K. I.; Vayssilov, G. N. Can the state of platinum species be unambiguously determined by the stretching frequency of an adsorbed CO probe molecule? *Phys. Chem. Chem. Phys.* **2016**, *18*, 22108–22121.

[69] Bazin, P.; Saur, O.; Lavalley, J. C.; Daturi, M.; Blanchard, G. FT-IR study of CO adsorption on Pt/CeO_2: Characterisation and structural rearrangement of small Pt particles. *Phys. Chem. Chem. Phys.* **2005**, *7*, 187–194.

[70] Li, J.; Tang, Y.; Ma, Y. Y.; Zhang, Z. Y.; Tao, F.; Qu, Y. Q. *In situ* formation of isolated bimetallic PtCe sites of single-dispersed Pt on CeO_2 for low-temperature CO oxidation. *ACS Appl. Mater. Interfaces* **2018**, *10*, 38134–38140.

[71] Ding, K. L.; Gulec, A.; Johnson, A. M.; Schweitzer, N. M.; Stucky, G. D.; Marks, L. D.; Stair, P. C. Identification of active sites in CO oxidation and water–gas shift over supported Pt catalysts. *Science* **2015**, *350*, 189–192.

[72] Peng, R. S.; Sun, X. B.; Li, S. J.; Chen, L. M.; Fu, M. L.; Wu, J. L.; Ye, D. Q. Shape effect of Pt/CeO_2 catalysts on the catalytic oxidation of toluene. *Chem. Eng. J.* **2016**, *306*, 1234–1246.

[73] Zhang, D. F.; Zhang, C. S.; Chen, Y. M.; Wang, Q. F.; Bian, L. Y.; Miao, J. Support shape effect on the catalytic performance of Pt/CeO_2 nanostructures for methanol electrooxidation. *Electrochim. Acta* **2014**, *139*, 42–47.

[74] Tong, T.; Liu, X. H.; Guo, Y.; Banis, M. N.; Hu, Y. F.; Wang, Y. Q. The critical role of CeO_2 crystal-plane in controlling Pt chemical states on the hydrogenolysis of furfuryl alcohol to 1,2-pentanediol. *J. Catal.* **2018**, *365*, 420–428.

[75] Wang, W. H.; Zhu, M. D.; Lu, X. L.; Gao, Y. F.; Li, L. J.; Cao, Z. Z.; Li, C. H.; Liu, J. R.; Zheng, H. T. Enhanced catalytic performance of a Pt-*x*CeO_2/graphene catalyst for DMFCs by adjusting the crystal-plane and shape of nanoscale ceria. *Rsc Adv.* **2015**, *5*, 74899–74906.

[76] Avanesian, T.; Dai, S.; Kale, M. J.; Graham, G. W.; Pan, X. Q.; Christopher, P. Quantitative and atomic-scale view of CO-induced Pt nanoparticle surface reconstruction at saturation coverage via DFT calculations coupled with *in situ* TEM and IR. *J. Am. Chem. Soc.* **2017**, *139*, 4551–4558.

[77] Zhao, E. W.; Zheng, H. B.; Zhou, R. H.; Hagelin-Weaver, H. E.; Bowers, C. R. Shaped ceria nanocrystals catalyze efficient and selective para-hydrogen-enhanced polarization. *Angew. Chem., Int. Ed.* **2015**, *54*, 14270–14275.